Beresovskaya, *Izv. Akad. Nauk SSSR Geol.* **12**, 86 (1978).

11. D. L. Bish and J. E. Post, *Geol. Soc. Am. Abstr. Prog.* **16**, 625 (1984).
12. J. Ostwald, *Mineral. Mag.* **50**, 336 (1986).
13. J. E. Post and D. L. Bish, *Am. Mineral.* **73**, 861 (1988).
14. R. G. Burns, V. M. Burns, H. W. Stockman, *ibid.* **68**, 972 (1983).
15. C. L. O'Young, in *Synthesis of Microporous Materials*, M. Occelli and H. Robson, Eds. (Van Nostrand Reinhold, New York, 1992), vol II, p. 333.
16. N. Yamamoto, T. Endo, M. Shimada, T. Takada, *Jpn. J. Appl. Phys.* **13**, 723 (1974).
17. O. Tamada and N. Yamamoto, *Mineral. J.* **13**, 180 (1986); N. Yamamoto and O. Tamada, *J. Cryst. Growth* **73**, 199 (1985).
18. R. M. McKenzie, *Mineral. Mag.* **38**, 294 (1971).
19. R. M. Porter and G. R. Rossman, *Am. Mineral.* **64**, 1199 (1979).
20. D. C. Golden, C. C. Chen, J. B. Dixon, *Clays Clay Miner.* **35**, 271 (1987).
21. ———, *Science* **231**, 717 (1986).
22. Y.-F. Shen, R. Zerger, S. L. Suib, L. McCurdy, D. I. Potter, C. L. O'Young, unpublished results.
23. S. Bach, M. Henry, N. Baffier, J. Livage, *J. Solid State Chem.* **88**, 325 (1990).
24. J. Pattanayak, V. Sitakara Rao, H. S. Maiti, *Thermochim. Acta* **151**, 193 (1989).
25. To synthesize Na$^+$-type oxides, Mn(OH)$_2$ sol was obtained by adding 50 ml of 5.0 M NaOH into 40 ml of 0.50 M MnCl$_2$ solution under vigorous stirring. The Mn(OH)$_2$ was then added dropwise to different amounts of 0.10 M Mg(MnO$_4$)$_2$ solution under vigorous stirring to prepare layered manganese oxides. The final pH for all sample suspensions was 13.8. The suspensions were aged at room temperature for 8 days and then filtered and washed with distilled deionized water (DDW) until no Cl$^-$ was detected. Mg^{2+}-type layered manganese oxides were obtained by ion-exchanging the Na$^+$-type layered manganese oxides with 1 liter of M MgCl$_2$ while stirring at room temperature overnight. The exchanged products were filtered and washed three times with DDW.
26. An aqueous sample suspension was put on a glass slide and dried in air at room temperature. XRD powder patterns were obtained with a Scintag XDS-2000 θ-θ diffractometer with Cu Kα radiation (45 kV and 40 mA). Two incident slits of 2 and 4 mm were used. Samples were ground to the same particle size. Voltages and currents were held constant for all experiments which were done in a 1-week period to avoid fluctuations in x-ray beam parameters. Complete XRD data summaries are available from the authors.
27. D. C. Golden, J. B. Dixon, C. C. Chen, *Clays Clay Miner.* **34**, 511 (1986).
28. R. DeGuzman, Y. F. Shen, S. L. Suib, B. R. Shaw, C. L. O'Young, in preparation.
29. The SEM/EDX spectra were taken in an AMRAY Model 1800D SEM equipped with PV9800 EDX spectrometer. An acceleration potential of 25 kV was used for the EDX measurements. Multispot analyses were done on different particles of a sample in order to obtain more accurate information regarding lateral and bulk homogeneity. Quantitative calculations were done with the Super Quant program with a ZAF correction to obtain relative concentrations.
30. G. M. Faulring, in *Advances in X-ray Analysis*, M. Mueller, Ed. (Plenum, New York, 1962), pp. 117–126.
31. Powdered samples were ground before they were dispersed into either acetone or ethanol and ultrasonically vibrated. Fine particles were then put onto a carbon-coated Cu grid for the TEM measurements. The TEM images and electron diffraction patterns were obtained with a Phillips EM-420 analytical electron microscope (AEM).
32. Thermal analyses of the air-dried samples were carried out with a DuPont 910 DSC. The TGA experiments were done in a DuPont 951 instrument. About 3- to 10-mg samples were used.
33. P. B. Weisz, *J. Catal.* **10**, 407 (1968).
34. The EPR spectra of a sample diluted with silica gel (S-157, Fisher Scientific) were obtained with a Varian E-3 EPR spectrometer at 9.05 GHz, 77 K, and 0.5 mW of power.
35. J. Rubio, E. Munoz, P. J. Boldu, O. Y. Chen, M. M. Abraham, *J. Chem. Phys.* **70**, 633 (1979).
36. H. W. de Wijn and R. F. van Balderen, *ibid.* **46**, 1381 (1967).
37. Cyclic voltammetry experiments were done on a BAS Model 100 electrochemical apparatus. (A saturated calomel electrode was used as a reference and a Pt wire was used as a counterelectrode.) Working electrodes of manganese oxide minerals and synthetic manganese oxides were prepared by taking 20 to 40% by weight manganese oxide and mixing it with carbon paste. Working electrodes were made by connecting the carbon paste manganese oxide mixtures to a copper wire. Electrolyte solutions were prepared from K and Na phosphate buffers of pH 5.0, 7.0, and 10.0 from pHydrion Buffers. Argon gas bubbled through the electrolyte solution for at least 10 min to remove oxygen gas. Several cycles were typically done in order to follow changes in reductions and oxidations on cycling.
38. A self-supported manganese oxide sample wafer was dehydrated in vacuum at 400°C for 3 hours. The sample wafer was then cooled to 100°C and exposed to pyridine vapor for 0.5 hours. Desorption was conducted at 100°, 200°, and 300°C each for 1 hour before IR spectra were recorded at room temperature with a GL-6020 Galaxy Series FT-IR spectrometer.
39. Oxidation of methane was carried out by using a 1/4 wave Evenson microwave cavity and by flowing CH$_4$ at a flow rate of 50 ml/min at a pressure of 20 torr in a quartz reactor that has previously been described [S. J. Suib and Z. Zhang, U.S. Patent 5 015 349 (1991); P. R. Zerger and S. L. Suib, *J. Catal.* **139**, 383 (1993)]. Synthetic todorokite was placed downstream of the plasma zone at ambient temperature. Products were analyzed on stream with gas chromatography methods. The thermal temperatures in the plasma are typically between 75° and 150°C. The electronic temperatures in the plasma are likely near 2000 K.
40. Compositions were analyzed with a Varian Techtron AA-6 atomic absorption spectrophotometer (AAS) with a nitrous oxide–acetylene flame. The standard for Mn was Mn metal dissolved in 5% nitric acid, which was diluted with 1% nitric acid. About 50 mg of synthetic todorokite sample dried at 120°C was dissolved with 20 ml of DDW, 1 ml of concentrated nitric acid, and 2 ml of 30% hydrogen peroxide. The colorless solution was boiled for 2 to 5 min to remove excess peroxide and the solution was diluted with DDW to 100 ml to make a stock solution. Manganese was analyzed by using the standard addition method.
41. J. M. Murray, L. S. Balistieri, B. Paul, *Geochim. Cosmochim. Acta* **48**, 1237 (1984).
42. We acknowledge the support of the Department of Energy, Office of Basic Energy Sciences, Division of Chemical Sciences, and Texaco, Inc. for support of this research. We thank A. Clearfield, J. Dixon, and L. R. Faulkner for helpful discussions. Helpful discussions with B. R. Shaw on electrochemical studies are appreciated. We thank C. Francis of the Harvard Mineralogical Museum for loan of various manganese oxide minerals including pyrolusite (cat. no. 100686), manganite (cat. no. 131562), hollandite (cat. no. 106790), birnessite (cat. no. 1007575), and todorokite (cat. no. 104794).

6 October 1992; accepted 21 January 1993

Vapor-Condensation Generation and STM Analysis of Fullerene Tubes

Maohui Ge and Klaus Sattler

Fullerene tubular structures can be generated by vapor condensation of carbon on an atomically flat graphite surface. Scanning tunneling microscope (STM) images revealed the presence of tubes with extremely small diameters (from 10 to 70 angstroms), most of which are terminated by hemispherical caps. Atomic resolution images of such structures showed that the tubes have a helical graphitic nature. The formation of the tubes under the quasi-free conditions suggests that the growth to tubular rather than spherical configurations is preferred for "giant fullerenes."

Despite the tremendous interest recently in the physics and chemistry of C$_{60}$ and other fullerenes and their solid forms, little is known about fullerene growth. Neither the onset of nucleation nor the progression toward the fullerene network is understood. The structure of giant fullerenes (containing hundreds of carbon atoms) is also controversial; experimental evidence exists to support two possibilities, spherical molecules versus tubular cages.

Concentric tubular carbon structures were recently found by transmission electron microscopy at the end of carbon rods used for arc discharge (*1*, *2*), and such structures could be produced in macroscopic quantities by using a similar generation method (*3*). The smallest inner tube that was observed (*1*) had a diameter of 22 Å. Electron diffraction pattern revealed helical arrangement for concentric graphitic networks. The tubes were grown out from a carbon substrate. Therefore a direct comparison to the free fullerene growth could not be made. Although various properties of the tubules were measured, the atomic structure could not be directly determined.

Recent calculations predict that carbon tubules of different diameters and helicities have striking variations in electronic transport, from metallic to semiconducting (*4*–*7*). Also, such tubules are expected to shield guest atoms from external electric and magnetic fields (*8*). Besides tubular structures, other low-energy configurations

---

Department of Physics and Astronomy, University of Hawaii, Honolulu, HI 96822.

such as negative-curvature fullerene analogs were also suggested (*9–11*).

We have produced carbon tubules by quasi-free vapor condensation. This method is different from the previously reported generation method of carbon tubes (*1, 2*). Atomic resolution images obtained with a scanning tunneling microscope (STM) reveal that the detailed structures of the tube surfaces are networks of perfect honeycombs. In addition, we observe a superpattern on the tubes due to an incorporated inner tube with different helicity. The smallest tube imaged in our experiments has a diameter of ~10 Å, which is of the size of C_{60}. We suggest that the tubule growth starts with the formation of a fullerene hemisphere.

Our samples were prepared by vapor deposition of carbon on highly oriented pyrolytic graphite (HOPG) in ultrahigh vacuum (UHV) at a base pressure of $\sim 10^{-8}$ torr. The use of graphite as a substrate might lead to problems of distinguishing adlayer features from steps, flakes, or other substrate features (*12*). This possibility, however, can be excluded with our preparation procedure. The graphite (grade-A HOPG) was freshly cleaved in UHV and carefully examined by STM before the deposition. The HOPG surface was atomically flat and defect-free over micrometer dimensions. It was cooled to −30°C during evaporation. The carbon vapor was produced by resistively heating a carbon foil. The deposition rate was monitored by a quartz crystal film-thickness monitor. The average thickness of the carbon adlayers ranged from 20 to 60 Å. After deposition, the samples were transferred to an STM operated at $\sim 10^{-10}$ torr without breaking vacuum. The STM imaging was performed at room temperature. The microscope was usually operated in the constant-current mode in which the tip-to-sample distance is kept constant by means of an electronic feedback control. The atomic-scale images were obtained in the variable-current mode. Bias voltages of 100 to 500 mV (both positive and negative) and tunneling currents of 0.5 to 3.0 nA were applied. A mechanically shaped Pt-Ir tip was used.

Carbon tubes with diameters between 10 Å and 70 Å and up to 2000 Å in length were found. Three STM images of such tubes are shown in Fig. 1. The cylindrical shape is well displayed. Whereas Fig. 1, A and B, shows parts of much longer tubes, Fig. 1C shows smaller ones. Most of the tubes are terminated by hemispherical caps. Two of them in Fig. 1B are broken at the lower left corner of the image.

In some cases we observed a coaxial arrangement of the outermost and an inner tube (upper right corner, Fig. 1B). The outer tube is terminated in this region, and the adjacent inner one is imaged simultaneously. We measure an interlayer spacing of 3.4 Å, which is about the graphite interlayer distance (3.35 Å). Such possible coaxial arrangement was confirmed by atomic-scale imaging.

We found that the tubes are placed almost horizontally on the substrate. Irregular nanostructures were also formed as displayed in the images. However, the high occurrence (>50%) of tubes clearly shows that the carbon atoms prefer to condense to tubular structures, as opposed to other nanostructures, under our preparation conditions.

In Fig. 2A we show an atomic resolution image of a carbon tube, 35 Å in diameter. The structure imaged at the upper right corner of the picture comes from another tube. Both of them were ~1000 Å long. A perfect honeycomb surface structure is observed. By taking into account the curvature of the tube surface and the STM imaging profile, we find the same lattice parameter as that of graphite (1.42 Å), demonstrating that the tubular surface is a graphitic network.

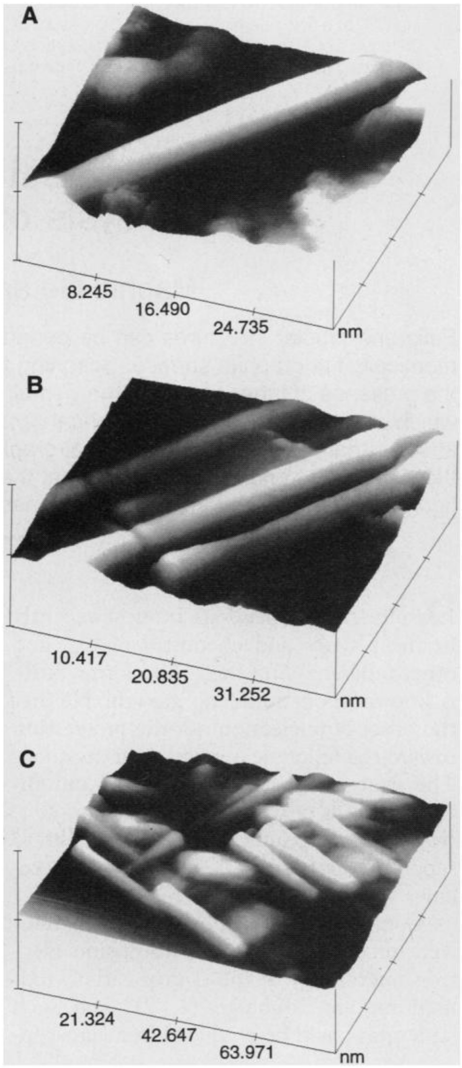

Fig. 1. Three STM images of fullerene tubes on a graphite substrate.

One question arises if the observed tubules are scroll-type filaments or perfect cylinders. Scroll-type filaments should have edge overlaps on their surfaces. During our extensive STM survey along the tube surfaces on the atomic scale, we did not observe any edges due to incomplete carbon layers. Therefore we conclude that the tubes are complete graphitic cylinders.

For the tube in Fig. 2A, the honeycomb surface net is arranged in a helical way. A chiral angle of 5.0° ± 0.5° is obtained. The chiral angle is defined as the smallest angle between the tube axis and the C–C bond directions of the honeycomb lattice. We determined the tube axis from a large-scale image.

For the formation of carbon tubes, spherical-type nucleation seeds seem to be required. In a common method for the production of tubular carbon fibers, the growth is initiated by submicrometer-size catalytic metal particles (*13*). Tube growth out of a graphite rod during arc discharge might also be related to nanoparticle-like seeds present at the substrate (*2*). Under conditions that resemble those for the production of fullerenes, another type of nucleation seed is possible. In this case, the tubes may grow out of a hollow fullerene cap rather than out of a compact spherical particle. After one-half of a fullerene is formed, the subsequent growth can proceed to a tubular structure rather than to a spherical cage.

Indeed, the smallest tube that we measured had a diameter of 10 Å, which is of the size of C_{60}. It is predicted to be the limiting case of vapor-grown graphitic tubes with monolayer thickness (*14*). Our observation of hemispherically capped 10 Å tubes suggests that an incomplete C_{60} cluster is the nucleation seed for these tubes. The C_{60}-derived tube could be the core of possible multilayer concentric graphitic tubes. After the fullerene-based tube has been formed, further concentric shells can be added by graphitic cylindrical layer growth.

A "ball-and-stick" model of a C_{60+10j} ($j = 1, 2, 3, \ldots$) tube with C_5 symmetry (Fig. 2B) yields a diameter of 6.83 Å. By considering the charge distribution, the resulting outer diameter is 9.6 Å (*14*), which is nearly the same as the smallest one observed in our experiment. In the model, one end of the tube is closed by a C_{60} hemisphere. The cap contains six pentagons, and the body part of the tube contains only hexagons. The hexagonal rings are arranged in a helical fashion with a chiral angle of 30° ("armchair configuration"). One obtains this result when the tube axis is the fivefold symmetric axis of the C_{60} cap. Other choices of symmetry axes for C_{60}

caps lead to slightly larger tube diameters and different helicities.

For the structural consideration, the graphitic monolayer tube can be treated as a rolled-up graphite sheet that matches perfectly at the closure line. Choosing the cylinder joint in different directions leads to different helicities. One single helicity gives a set of discrete diameters. In order to obtain the diameter that matches exactly the required interlayer spacing, the tube layers need to adjust their helicities. Therefore, in general, different helicities for different layers in a multilayer tube are expected and were indeed found in our experiment.

In Fig. 2A we observe a zigzag superpattern in addition to the atomic lattice. It appears along the axis at the surface of the tube. The zigzag angle is 120°, and the period is ~16 Å. This superstructure can be considered as part of a honeycomb-type giant lattice. Such giant lattices have been observed for plane graphite when imaged by STM (*15–20*). They can be explained by misorientation of the top layer relative to the second layer (*15–17*), which results in a Moire pattern with the same type of lattice structure but a much larger lattice parameter. The angle of misorientation determines the lattice constant. Because of the nonequivalent atomic stacking, the local electron density of states at the Fermi level of the top layer is modulated (*16*). Therefore the STM can image a giant lattice in addition to the atomic lattice and can give the relative orientation of the first two layers. For multilayer tubes with different helicities between the top and the second layer, one expects such a superpattern to be observed. The helicity of the second layer can be determined from the period of the superstructure.

However, while there is an analogy between two misoriented graphite sheets and two concentric cylindrical graphitic sheets of different helicity, there is also a difference. For planar sheets, the superpattern is extended throughout the whole plane, whereas for cylindrical sheets it should appear only within narrow stripes along the tube axis. This effect occurs because the curvature is different between the two cylinders, which affects the atomic stacking mainly in the direction perpendicular to the tube axis.

In Fig. 2C we illustrate a schematic model of such a superpattern. Two graphite sheets that are rotated relative to each other are superimposed, which results in a giant honeycomb lattice. By choosing an angle of 9° for the misorientation, we obtain a superlattice period of 16 Å.

In general, from such modeling one finds that for small chiral angles of both cylinders the tube axis is approximately along the zigzag direction of the giant honeycomb lattice. The zigzag superpattern along the

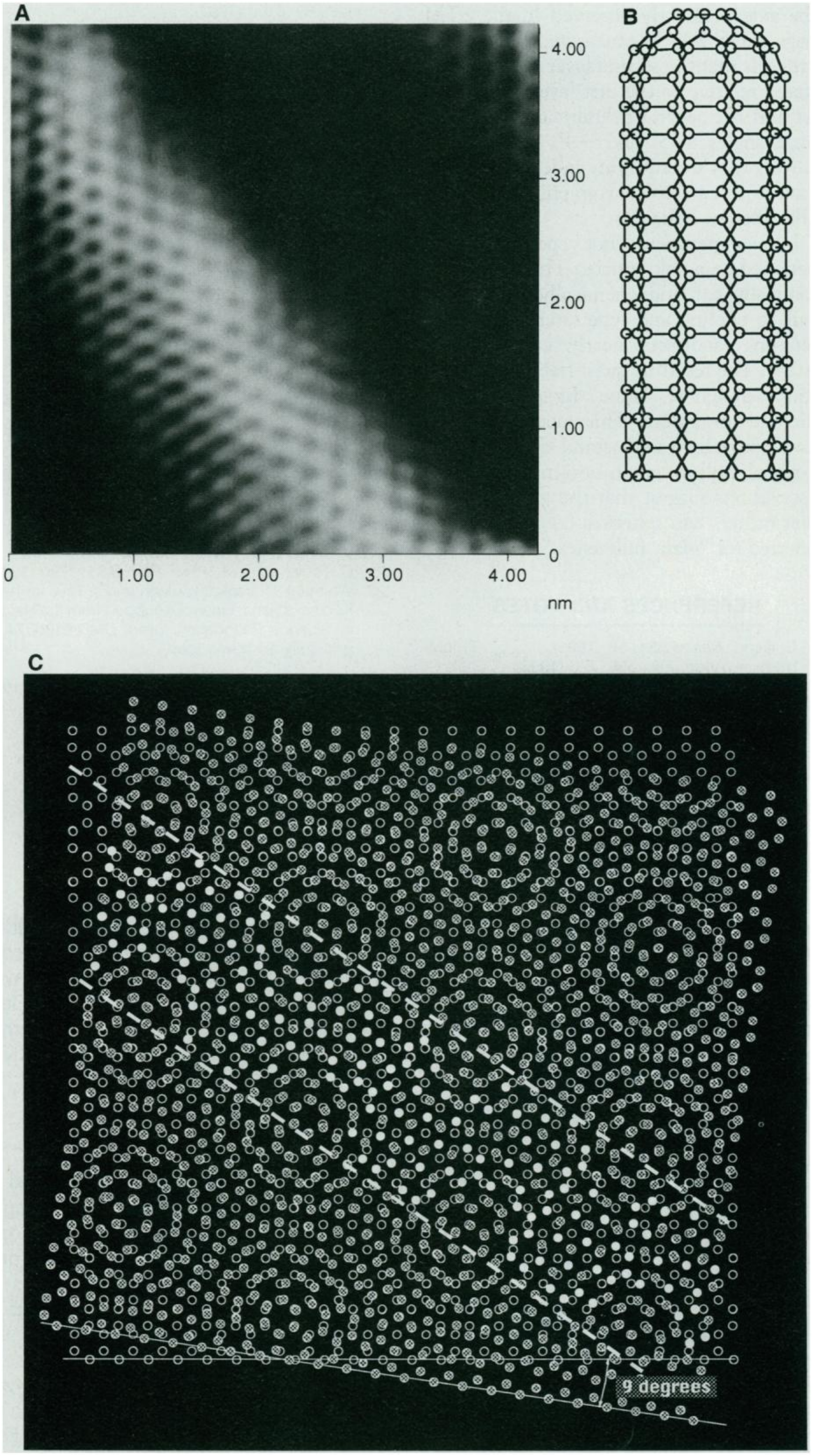

Fig. 2. (**A**) Atomic resolution STM image of a carbon tube, 35 Å in diameter. In addition to the atomic honeycomb structure, a zigzag superpattern along the tube axis can be seen. (**B**) "Ball-and-stick" structural model of a C_{60}-based carbon tube. The upper part is closed by a C_{60} hemisphere cap. (**C**) Structural model of a giant superpattern produced by two misoriented graphitic sheets. The carbon atoms in the first layer are shaded, and the second layer atoms are open. Between the two dashed lines, we highlight those first layer atoms with white that do not overlap with second layer atoms. Because of their higher local density of states at the Fermi level, these atoms (β-type atoms) appear particularly bright in STM images (*16, 21*). It results in a zigzag superpattern along the tube axis within the two white dashed lines as indicated.

tube axis is directly observed in the STM image of Fig. 2A. The measured period of 16 Å reveals that the second layer of the tube is rotated relative to the first layer by 9°. The first and the second cylindrical layers have chiral angles of 5° and −4°, respectively, showing that the tubes are indeed composed of at least two coaxial graphitic cylinders with different helicities.

In our experiments, hot vapor is suddenly quenched on a cold surface. The substrate is atomically flat and chemically inert. This leads to cooling and supersaturation of the incoming vapor on a nearly noninteracting surface. The resulting quasi-free growth conditions resemble those for vapor-phase fullerene formation. This method gives a new approach to understand the formation of novel hollow graphitic structures. Our observations suggest that the growth to tubular rather than spherical configurations is preferred for "giant fullerenes."

REFERENCES AND NOTES

1. S. Iijima, *Nature* **354**, 56 (1991); ______, T. Ichihashi, Y. Ando, *ibid.* **356**, 776 (1992).
2. S. Iijima, P. M. Ajayan, T. Ichihashi, *Phys. Rev. Lett.* **69**, 3100 (1992).
3. T. W. Ebbensen and P. M. Ajayan, *Nature* **358**, 220 (1992).
4. R. Saito, M. Fujita, G. Dresselhaus, M. S. Dresselhaus, *Appl. Phys. Lett.* **60**, 2204 (1992).
5. N. Hamada, S. Samada, A. Oshiyama, *Phys. Rev. Lett.* **68**, 1579 (1992).
6. J. W. Mintmire *et al.*, *ibid.*, p. 631.
7. K. Harigaya, *Phys. Rev. B* **45**, 12017 (1992).
8. M. Peterson and J. Q. Broughton, *Phys. Rev. Lett.* **69**, 2689 (1992).
9. T. Lenosky *et al.*, *Nature* **355**, 333 (1992).
10. D. Vanderbilt and J. Tersoff, *Phys. Rev. Lett.* **68**, 511 (1992).
11. M. O'Keeffe *et al.*, *ibid.*, p. 2325.
12. C. R. Clemmer and T. P. Beebe, Jr., *Science* **251**, 640 (1991).
13. G. Tibbetts, *J. Cryst. Growth* **66**, 632 (1984).
14. M. S. Dresselhaus, G. Dresselhaus, R. Saito, *Phys. Rev. B* **45**, 6234 (1992).
15. M. Kuwabara, D. R. Clarke, D. A. Smith, *Appl. Phys. Lett.* **56**, 2396 (1990).
16. J. Xhie, K. Sattler, M. Ge, N. Venkatasmaran, *Phys. Rev. B*, in press.
17. P. I. Oden *et al.*, *Surf. Sci. Lett.* **254**, L454 (1991).
18. J. W. Lyding *et al.*, *J. Vac. Sci. Technol.* **A6**, 363 (1988).
19. J. E. Buckley *et al.*, *ibid.* **B9**, 1079 (1991).
20. V. Elings and F. Wudl, *ibid.* **A6**, 412 (1988).
21. D. Tomanek *et al.*, *Phys. Rev. B* **35**, 7790 (1987).

22. We thank N. Venkateswaran and J. Xhie for helpful discussions. Financial support from the National Science Foundation, grant DMR-9106374, is gratefully acknowledged.

21 December 1991; accepted 16 February 1993

Oxygen Diffusion in Perovskite: Implications for Electrical Conductivity in the Lower Mantle

Bjarni Gautason and Karlis Muehlenbachs

Experimental determination of oxygen self-diffusion in $CaTiO_3$ perovskite, a structural analog of $(Mg,Fe)SiO_3$ perovskite, confirms a theoretical relation between diffusion constants and anion porosity. Oxygen diffusion rates in $(Mg,Fe)SiO_3$ perovskite calculated with this relation increase by about eight orders of magnitude through the lower mantle. Electrical conductivity values calculated from these diffusion rates are consistent with inferred conductivity values for the lower mantle. This result suggests that the dominant conductivity mechanism in the deep mantle is ionic.

The lower mantle is the Earth's largest silicate and oxygen reservoir, constituting roughly half of the planet's volume. The dominant phase in the lower mantle, $(Mg,Fe)SiO_3$ perovskite, accounts for >85% of its volume (*1*). Consequently, diffusion of major elements in this phase may dominate dynamic processes in the lower mantle. Only recently have measurements of the physical properties of $(Mg,Fe)SiO_3$ perovskite at pressures and temperatures that correspond to those of the lower mantle become possible (*2, 3*). These measurements are still limited because of sample size and constraints of the experimental apparatus. In the absence of direct experimental determination, diffusion rates at very high pressure and temperature may be inferred by experimental study of analog phases, empirical modeling, or theoretical calculations. The data from these approaches may provide a framework to discuss subjects such as isotopic equilibration rates, mantle rheology, chemical transfer between mantle and core, and ionic conductivity.

In this report we provide data on oxygen diffusion in $CaTiO_3$ perovskite, a phase commonly used as an analog to $(Mg,Fe)SiO_3$ perovskite (*4*). Both $CaTiO_3$ and $(Mg,Fe)SiO_3$ perovskite are orthorhombic ABO_3 compounds, with a similar tolerance factor (*5*) and, hence, similar thermochemical properties (*6*). The experimentally determined oxygen diffusion constants for $CaTiO_3$ are consistent with empirical rules that relate diffusion constants to crystal porosity (*7*). Therefore, we propose that the empirical relations may be used to estimate oxygen diffusion constants for $(Mg,Fe)SiO_3$ perovskite.

Diffusion is a thermally activated process and is commonly described by the Arrhenius relation

$$D = D_0 \exp(-Q/RT) \qquad (1)$$

where D is the diffusion coefficient, D_0 is a constant, Q is the activation energy, R is the gas constant, and T is absolute temperature. When this relation holds, a plot of the logarithm of the diffusion coefficients versus the inverse temperatures yields a straight line. To measure oxygen diffusion in $CaTiO_3$ perovskite, we partially equilibrated aliquots of perovskite powder with CO_2 gas at temperatures between 900° and 1300°C in a 1-atm furnace. Several experiments were done at each temperature, with varied grain size and run time (*8*). The data from our experiments (Fig. 1) fit an Arrhenius relation with an activation energy (derived from the slope on Fig. 1) of 313 ± 10 kJ mol^{-1} and a preexponential factor D_0 of $5.0^{+7.8}_{-3.1}$ cm^2 s^{-1}.

The experimentally derived oxygen diffusion constants Q and D_0 for $CaTiO_3$ perovskite are consistent with a recent empirical model that relates the activation energy for oxygen diffusion and the preexponential factor ($\ln D_0$) to the anion porosity (Φ) of crystals (*7*). The anion porosity is a measure of the volume fraction not occupied by anions and is defined as $1 - (V_A/V)$, where V_A is the volume of anions in the unit cell and V is the unit cell volume (*9*). Data from 1-atm oxygen diffusion experiments on several minerals (Table 1) illustrate a well-defined linear relation (Fig. 2A) between anion porosity and the activation energy. In contrast, the relation between porosity and $\ln D_0$ (Fig. 2B) shows considerable scatter. In both plots, the scatter is significantly reduced if the data from a single laboratory are considered (*7*), which suggests that some scatter stems from interlaboratory comparison. Furthermore, the activation energy and $\ln D_0$ cannot be determined independently, and small uncertainties in the slope (Q) will lead to large uncertainties in D_0.

The linear relations may be combined to give an equation that relates anhydrous oxygen diffusion to temperature and anion porosity (*7, 10*)

$$\ln D = A + B\Phi - [(L + M\Phi)10^3/RT] \qquad (2)$$

The constants A and B are the intercept and slope, respectively, in the linear relation between $\ln D_0$ and Φ, and the relation between Q and Φ is similarly described by the constants L and M (Fig. 2, A and B). We obtained $A = 36.5 \pm 7.7$, $B = -1.01 \pm 0.17$, $L = 1116 \pm 60$, and $M = -18.6 \pm 1.3$ from the values in Table 1 (*11*). The

---

Department of Geology, University of Alberta, Edmonton T6G 2E3, Canada.